Scientific Journals
of the Maritime University of Szczecin

Zeszyty Naukowe
Akademii Morskiej w Szczecinie

2019, 60 (132), 9–17
ISSN 1733-8670 (Printed)
ISSN 2392-0378 (Online)
DOI: 10.17402/366

Received: 02.10.2019
Accepted: 22.11.2019
Published: 18.12.2019

Parametric study on the flow field generated by river barge bow steering systems

Teresa Abramowicz-Gerigk✉, Zbigniew Burciu, Jacek Jachowski

Gdynia Maritime University, Department of Ship Operation
81-87 Morska St., 81-225 Gdynia, Poland
e-mail: {t.gerigk; z.burciu; j.jachowski}@wn.umg.edu.pl
✉ corresponding author

Key words: Magnus effect, bow rotor steering system, river barge, flow field, CFD

Abstract
Low controllability under strong winds presents a problem for the operation of inland vessels, which can be improved using passive bow rudders and transverse thrusters. Bow thrusters can sufficiently improve the manoeuvrability at low speeds, but an unsolved problem is course maintaining and yaw checking of a vessel at medium and high speeds. This paper proposes the use of a bow steering system in which the bow rotors generate a Magnus force. The first physical test model of the system showed promising results and that much more research must be performed before this system can be used in industrial applications. The paper presents the results of a numerical study on the flow field generated by bow rotors. The first stage of a ship's turn using the bow rotors was used to determine the dependence of the expected steering force on the inflow velocity and rotational speed of the rotors. The influence of the flow generated by the bow steering system on river banks and quay walls during manoeuvres was also discussed.

Introduction

Inland navigation primarily occurs in restricted waters with navigational limits due to shallow water, under-bridge clearances, and narrow winding waterways with alternating currents. The main factor influencing the safety of inland navigation is the width of the safe manoeuvring area – the width of the lane and good vessel manoeuvrability during the entire voyage over a wide speed range.

Inland fleet ship-owners continuously seek new technologies to improve the manoeuvring characteristics of inland vessels. An unsolved problem is how to control motions of shallow-draft vessels under strong winds at medium or high vessel speeds. The bow steering system described in this paper can reduce the required lane width and bend radius due to improved ship manoeuvrability. Previous investigations using a physical model on a 1:20 scale of a river push barge (Abramowicz-Gerigk, Burciu & Jachowski, 2017; Abramowicz-Gerigk & Burciu, 2018) gave very promising results related to the increased manoeuvrability of a pushed train and have become the subject of interest of the largest Polish ship-owner.

The main problem related to commercialization of the bow steering system is Magnus lift force control. The available published results which have investigated rotor dynamics have mainly considered aerodynamic phenomena at low Reynolds numbers (Catalano et al., 2003; Champmartin, Ambari & Roussel, 2007; Everts et al., 2014; Rao et al., 2014; Yao, Zhou & Wang, 2016; Pullin, Cheng & Samtaney, 2018). For instance, Karabelas et al. (Karabelas et al., 2012) used the results of a CFD study to propose an empirical method to determine the lift force generated on a rotor in the air at $Re = 10^5$, $Re = 10^6$, and $Re = 5 \cdot 10^6$, which corresponded to the Reynolds numbers of rotors in a river barge steering system.

This paper presents a possible application area of the proposed steering system and a parametric study of the flow field generated by bow rotors in the first stage of vessel turning. The dependence of Magnus force on bow rotor revolutions and push train speed was investigated. This study also includes a discussion on the influence of the bow rotor on a quay wall or river bank compared with a bow thruster.

Manoeuvrability of the units operated in inland waterborne transport

The systems used in inland waterborne freight transport can be categorized depending on the type of propulsion forces they use, e.g. river current, own drive, pushing or towing force (self-floating down a river system, self-propelled motor barge, and towing and pushing units). The most basic system is a pushing unit (pushed train or convoy), which is comprised of pusher and pushed barges (Figure 1).

Due to several advantages, pushed systems nearly made towed systems obsolete (Lantz et al., 2018). Pushed trains have several advantages compared with self-propulsion and towing systems, including a lower resistance related to loading capacity, fewer crew members, the ability to use different pushed barge formations, and lower pushed barge construction costs.

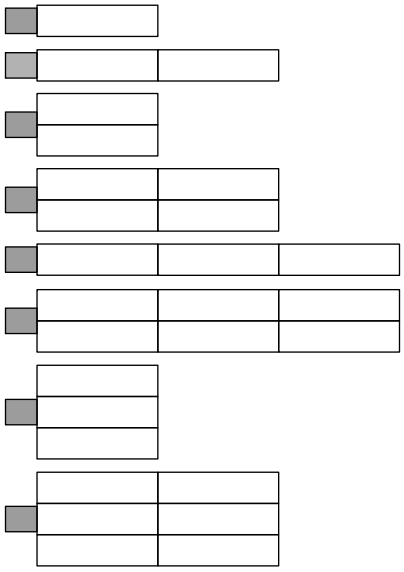

Figure 1. Pushed trains, examples of combinations of barges in pushed systems

Manoeuvring space of inland waterborne transport units – lane width

The main factors related to the safe lane in river transport are as follows (PIANC, 2019): factors related to the ship manoeuvrability, fairway bounding by banks, type of seabed, wind speed, transverse water current, and navigational markings.

The vessel breadth and drift angle resulting from ship motions under hydrometeorological conditions are the main ship manoeuvrability parameters which would necessitate increasing the width of a lane. The drift angle is defined as the angle between the ship centre line and velocity vector, or between the real ship course and its path over the water. The drift angle depends on wind speed, bend radius, propulsion power, loading condition of the pushed train, and the speed and direction of the pushed train down or up the river.

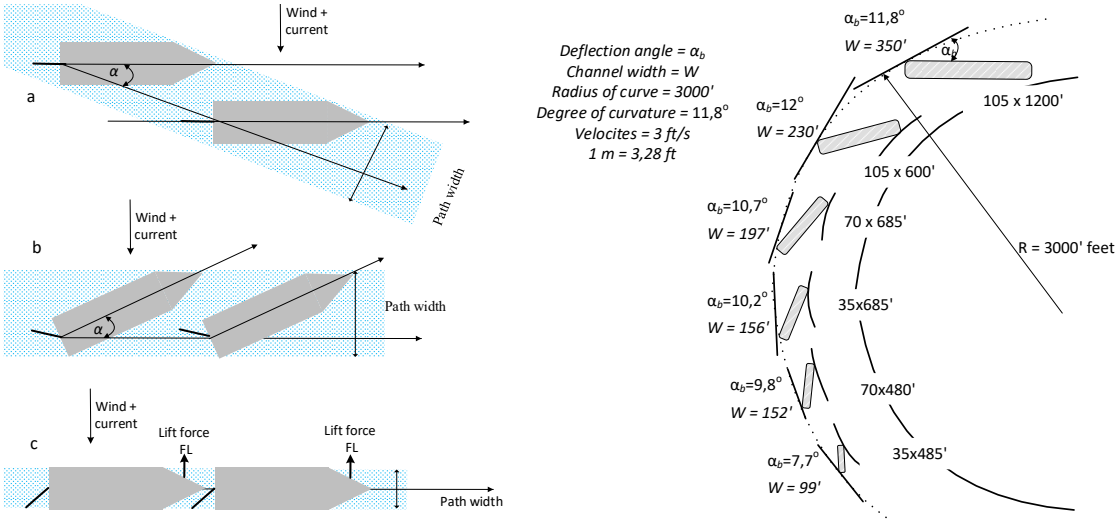

Figure 2. Increase in the manoeuvring path width due to hydrometeorological conditions: (a) no ship reaction to the drift, (b) pitch adopted to the drift, (c) reduction of the path width due to drift angle reduction by the steering force applied at the bow, (d) the drift angle α_b of convoys moving down the river in a bend with a ~900 m radius

Reducing the drift angle and improving turning characteristics of a push train are possible when additional steering forces are generated in forward motion. The most effective solution is the use of a bow steering system. An increase in the safe manoeuvring path width due to hydrometeorological conditions and possibly reducing the path width due to the drift angle reduction by a steering force applied at the bow is presented in Figure 2 a, b, c. The decreased drift angle can significantly enhance the safety of manoeuvres. The drift angles of convoys of various dimensions moving down the river in a bend with a 3000 feet (about 900 m) radius are presented in Figure 2d (Julien, 1997).

Manoeuvrability of a pushed convoy with a bow steering system

Auxiliary steering systems used to enhance push train manoeuvrability include passive bow rudders and tunnel thrusters installed on the first pushed barge in a convoy or on the independent floating modules equipped with bow thrusters that can be connected to the first barge. The limits of the passive and active systems are the small steering force of a bow rudder and a small range of velocities at which the steering force can be generated. The high power of the active units is also negatively affected by the river environment, construction, and other vessels. An illustration comparing the performance of a bow thruster and hydrodynamic rotor is presented in Figure 3. The thrust ratio is defined as the thrust at a given ship speed divided by the maximum possible thrust.

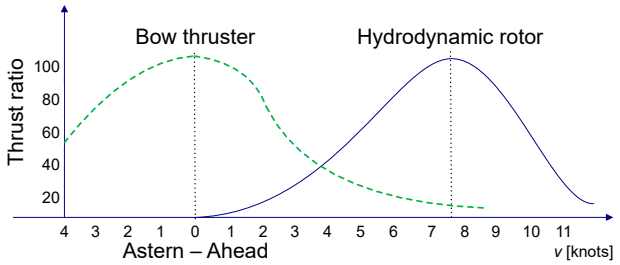

Figure 3. Thrust ratio as a function of the speed of a 150 m length vessel (Dymarski, Wieliczko & Nalewajski, 2003), compared with the efficiency of bow rotors as a function of speed of the 100 m length pushed train (Abramowicz-Gerigk, Burciu & Jachowski, 2017)

Bow steering system based on Magnus Effect

The steering force direction generated by rotors is related to the direction of the inflow velocity and depends on the pushed train velocity direction and rotor positions. The model tests presented in (Abramowicz-Gerigk, Burciu & Jachowski, 2017; Abramowicz-Gerigk & Burciu, 2018) confirmed that the steering force generated by rotors strongly influences the pivot point position during manoeuvres. The results of turning tests carried out for a 100 m long pushed train model in a 1:20 scale – performed using various combinations of stern rudders, bow rotors, and a dynamic coupling system – are presented in Figure 4.

Figure 5 presents the influence of a decreased drift angle due to bow rotor operation on manoeuvring path width during navigation on a straight course as a function of Δd and during an evasive manoeuvre (lateral displacement).

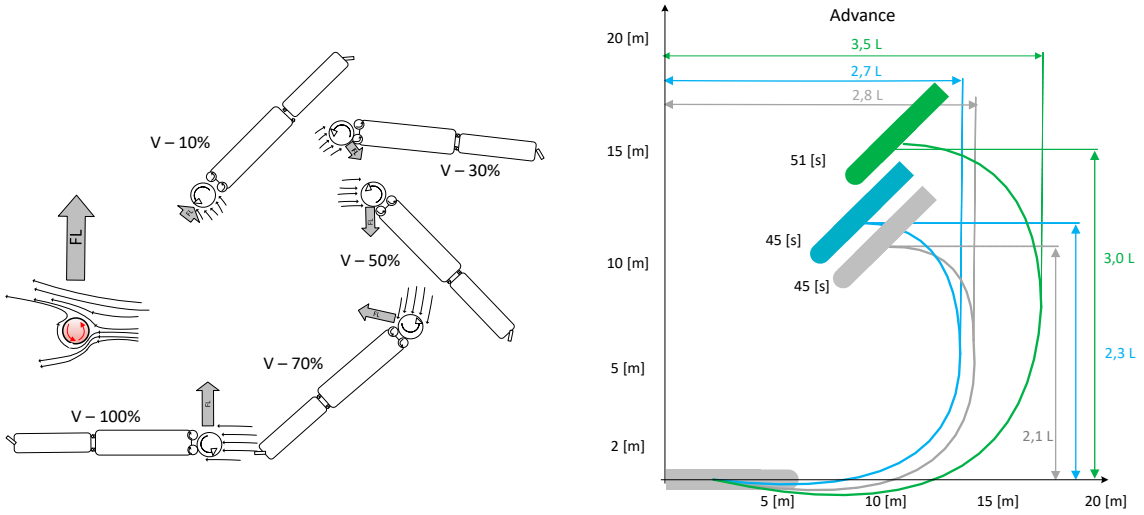

Figure 4. Turning using hydrodynamic bow rotors and main rudders – changes in the lift force related to changes in the inflow speed and direction. Turning manoeuvre of the pushed train using bow rotors (green); stern rudders and bow rotors (blue); stern rudders, bow rotors, and dynamical coupling system (grey)

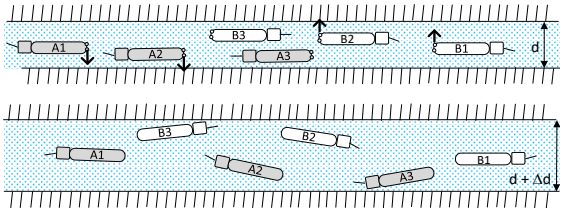

Figure 5. Required waterway width for navigation in a fixed course – evasive manoeuvre of pushed trains navigating with and without the use of hydrodynamic bow rotors

Parametric study on the lift force generated by a bow steering system

The Magnus effect is a phenomenon in which a lift force is generated perpendicular to the flow direction or to the motion direction of a fluid acting on a rotating cylinder or other rotational body. The theoretical value of the force in an incompressible fluid is determined by the Kutta-Joukowski law, which states that if an incompressible fluid flows around an infinitely long cylinder whose axis is perpendicular to the direction of the undisturbed flow, the lift force calculated per cylinder length unit can be defined by Equation (1):

$$F_L = \rho \cdot (v \times \Gamma) \tag{1}$$

where F_L is the lift force (N), ρ is the fluid density (kg/m^3), v is the relative speed of the fluid (m/s), and Γ is the rotation speed along a closed contour around the cylinder (m/s^2) (2):

$$\Gamma = 2\pi a^2 r \tag{2}$$

where a is the rotor radius [m], and r is the rotational speed of the cylinder [rad/s].

The lift force calculated for steady inviscid flow using Formula (1) is greater than the expected real mean force which varies with respect to the flow separation, edge losses, interaction effects, changes in the inflow velocity, and direction.

Based on a CFD study, Karabelas et al. (Karabelas et al., 2012) used Equation (3) to predict the lift force generated on a rotor in the air at high Reynolds numbers (10^5, 10^6, $5 \cdot 10^6$). This formula can be used to calculate the lift force of a fully-submerged rotor in the absence of a free surface effect:

$$F_L = C_L \cdot \rho \cdot v^2 \cdot a \tag{3}$$

where $C_L(\mathrm{Re}, \alpha)$ is the lift force coefficient (Karabelas et al., 2012), the Reynolds number Re is defined as $\mathrm{Re} = v \cdot 2a/\upsilon$, where υ is the kinematic viscosity of the fluid, and α is defined as:

$$\alpha = r \cdot a / v \tag{4}$$

Real conditions can be modelled using CFD simulations which allows the flow field pattern around the rotating cylinder to be observed and determines the lift force on a rotor under real conditions, including the influence of rotor geometry, motion parameters, and free surface effect. The tested geometry and motion parameters were assumed based on previous model tests (Abramowicz-Gerigk, Burciu & Jachowski, 2017; Abramowicz-Gerigk & Burciu, 2018).

Lift force generated on a rotor in open water conditions

The lift forces F_L calculated from Equation (3) for an assumed water density ρ = 1000 kg/m^3, kinematic viscosity $1.1 \cdot 10^{-6}$ Pa·s, v = 2.8 m/s, r = 40 rad/s, a = 0.25 m, and a = 0.5 m, H/D = 1 and H/D = 2 ($D = 2 \cdot a$) were compared with the mean/maximum lift forces $F_{L\mathrm{mean}}/F_{L\mathrm{max}}$ calculated using CFD simulations (FlowVision 2.5). The results are presented in Table 1.

Table 1. Lift forces calculated from Equation (3) and CFD simulations for a = 0.25 and a = 0.5 m

a	v	Re	r	H	α	H/D	$\lvert F_L \rvert$ (3)	$\lvert F_{L\mathrm{mean}} \rvert$ (CFD)	$\lvert F_{L\mathrm{max}} \rvert$ (CFD)
m	m/s	–	rad/s	m	–	–	kN	kN	kN
0.25	2.8	1.11	40	1	3.57	2	5.9	3.25	3.3
0.5	2.8	2.23	40	1	7.14	1	16.7	4.5	7.0

Doubling the rotor radius resulted in a 2.8 times greater lift force F_L, 1.4 times greater $F_{L\mathrm{mean}}$, and 2.12 times greater $F_{L\mathrm{max}}$. The rotor aspect ratio also significantly influences the lift force. $F_{L\mathrm{max}}$ calculated for the rotors with aspect ratios H/D = 2 and H/D = 1.0 using CFD are almost twice as small as the values obtained from Equation (3) for the rotor of infinite length, due to both edge losses and the free surface effect, as illustrated in Figure 6.

The free surface effect for a rotor of a = 0.5, H/D = 1, r = 40 rad/s, positioned 0.2H below the free surface and for two inflow velocities of 2.8 m/s and 5.6 m/s is presented in Figure 7.

The time series of rotational speed and generated lift forces are presented in Figure 8.

The lift forces calculated from Equation (3) for $\mathrm{Re} = 2.21 \cdot 10^6$ and $\mathrm{Re} = 4.43 \cdot 10^6$, α = 7.2 and α = 3.6 were equal to 19.3 kN and 51.0 kN. The effect of a free surface is greater at higher flow velocities, and the maximum forces calculated using CFD simulations were 2.8 kN and 4.9 kN, respectively. The lift

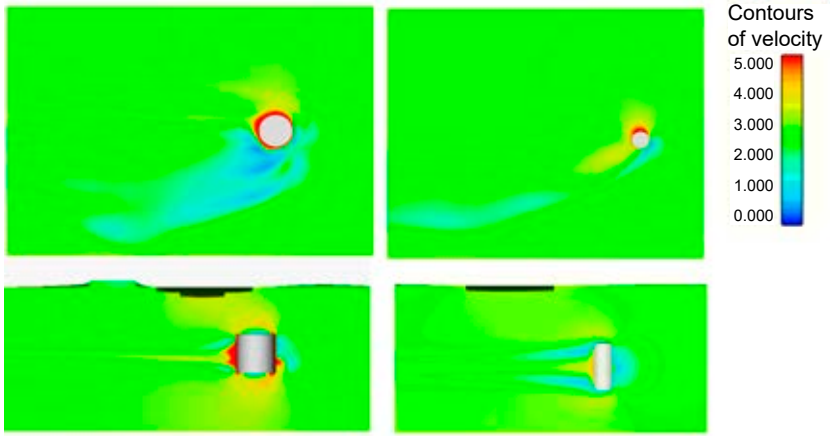

Figure 6. Flow velocity field generated by rotor, r = 40 rad/s, inflow velocities: v = 2.8 m/s, a = 0.5 m (left) and a = 0.25 m (right), Re = $1.11 \cdot 10^6$ and Re = $2.23 \cdot 10^6$, α = 3.57 and α = 7.14, respectively

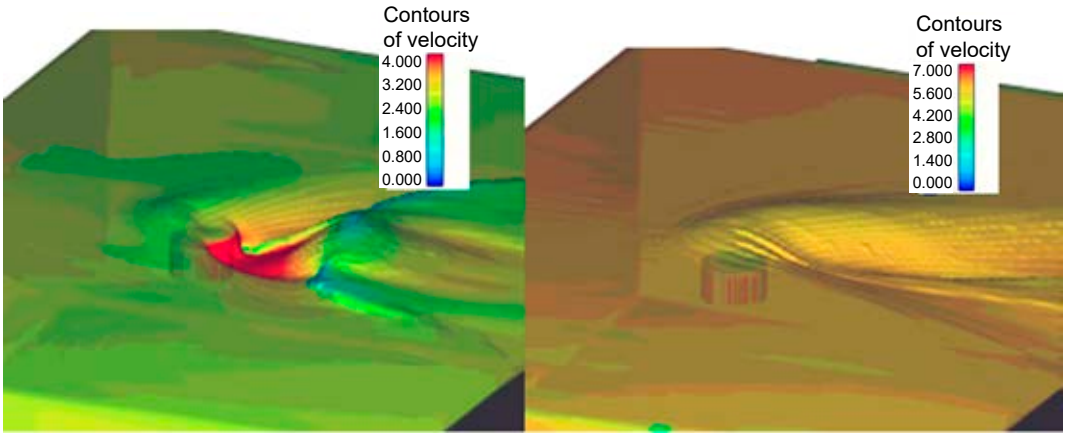

Figure 7. Flow velocity field generated by a rotor positioned 0.2H below the free surface: a = 0.5, H/D = 1, r = 40 rad/s, inflow velocities: v = 2.8 m/s (left) and v = 5.6 m/s (right)

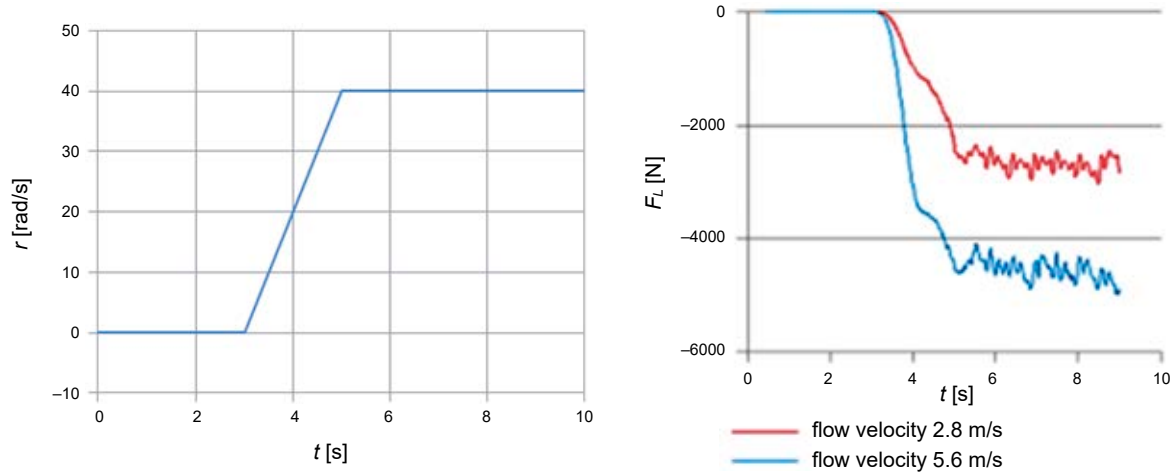

Figure 8. Time series of a rotor rotational speed r [rad/s], hydrodynamic lift forces generated by the rotor positioned 0.2H below the free surface: a = 0.5, H/D = 1, r = 40 rad/s, inflow velocities 2.8 m/s (red line) and 5.6 m/s (blue line)

forces began to increase at α = 3.6 (r = 20 rad/s) for both velocities and reached constant values at r = 40 rad/s, α = 7.2 for v = 2.8 m/s and α = 3.6 for v = 5.6. The lift forces calculated by taking into account the free surface effect at α = 7.2 and 3.6 are presented in Table 2.

Doubling the inflow velocity also causes the lift force to double in open water conditions. When the lift force was dominated by the free surface effect, this ratio was about 1.5. In both cases, v = 2.8 m/s and v = 5.6 m/s. $F_{L\text{mean}}$ is about ten times smaller than for a rotor of infinite length in open water conditions.

Table 2. Lift forces calculated using Equation (3) and CFD simulation taking into account the free surface effect at α = 7.2 and 3.6

a	v	Re	r	α	$\lvert F_L \rvert$ (3)	$\lvert F_{L\text{mean}} \rvert$ (CFD)	$\lvert F_{L\text{max}} \rvert$ (CFD)
m	m/s	–	rad/s	–	kN	kN	kN
0.5	2.8	2.21	40	7.20	19.3	2.7	2.8
0.5	5.6	4.43	40	3.60	51.0	4.5	4.9

Lift forces generated by rotors of a bow steering system

CFD simulations were carried out for a push train of 86 m length, 11 m breadth, 2 m depth, and 0.75 m draft, using an assumed water depth of 2 m and a water depth-to-draft ratio of 2.7 (Figure 9). The rotors in the bow were positioned on PS and STB sides within the hull form contour.

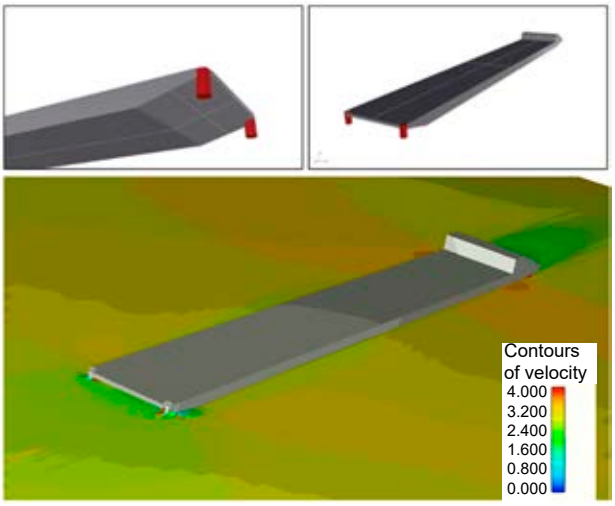

Figure 9. The bow rotors installed on port and starboard sides of the barge

The height of the rotor was 1 m, which was submerged up to 0.77 in calm water. The parametric study included three push train velocities (2 m/s, 3 m/s, and 4 m/s), two rotor radii of 0.465 m and 0.25 m, and rotational speeds related to the inflow velocities of α = 4.44, 5.67, and 7.50. The influence of the rotational speed of bow rotors and barge velocity on the lift force is presented in Figures 10, 11, and 12.

The mean lift forces acting on PS and STB rotors calculated using CFD simulation were 200 N and 250 N, respectively.

The different lift force directions on the port and starboard rotor at r = 0 rad/s were determined using different flow distributions with respect to the

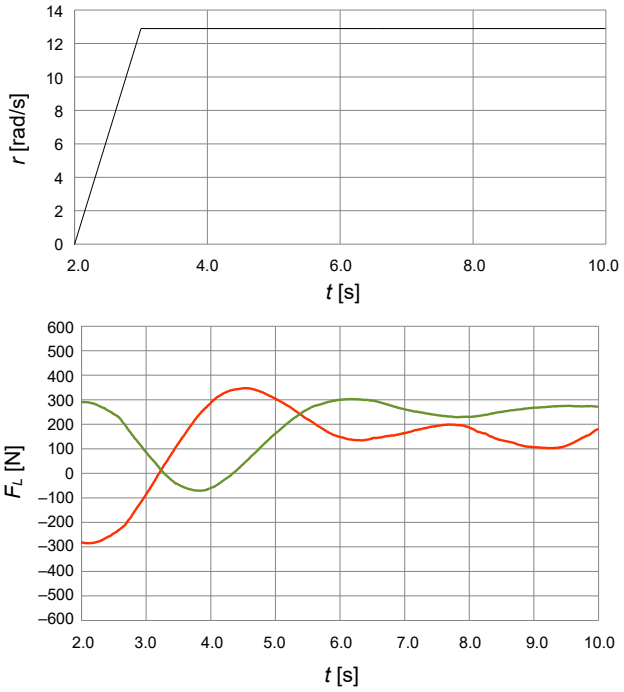

Figure 10. Time series of the rotational speed of rotors and hydrodynamic lift forces generated by the PS (red line) and STB (green line) rotors: a = 0.465, barge velocity v_{barge} = 2 m/s, α = 4.44

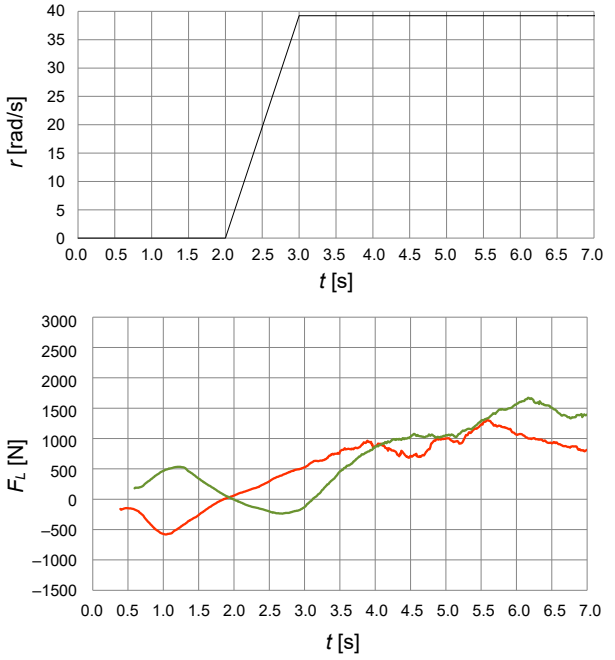

Figure 11. Time series of the rotational speed of rotors and hydrodynamic lift forces generated by the PS (red line) and STB (green line) rotors, inflow velocity v_{barge} = 3 m/s, α = 7.50

influence of the hull and bow wave. The mean lift forces calculated using CFD simulations on PS and STB rotors were 1.0 kN and 1.5 kN, respectively.

The mean lift forces calculated using CFD simulations on PS and STB rotors were 4.0 kN and

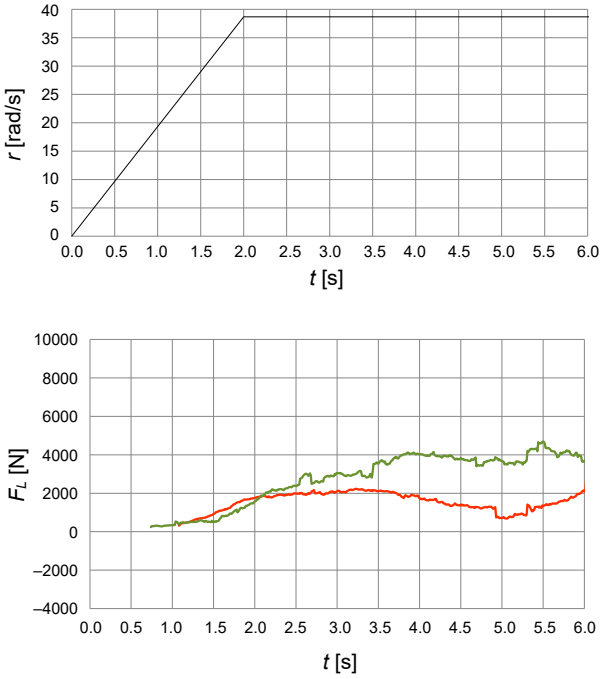

Figure 12. Time series of the rotational speed of rotors and hydrodynamic lift forces generated by the PS (red line) and STB (green line) rotors, barge velocity v_{barge} = 4 m/s, α = 5.67

2.0 kN, respectively, which are much smaller than those calculated for the open water conditions due to bow wave formation and interaction effects. The velocity fields generated at v_{barge} = 3 m/s for the rotor radii equal 0.25 m and 0.465 m (Figure 13).

The influence of variations in the rotor rotational speed on the lift force is presented in Figure 14.

The increase of the maximum lift forces can be observed for α greater than 5.21.

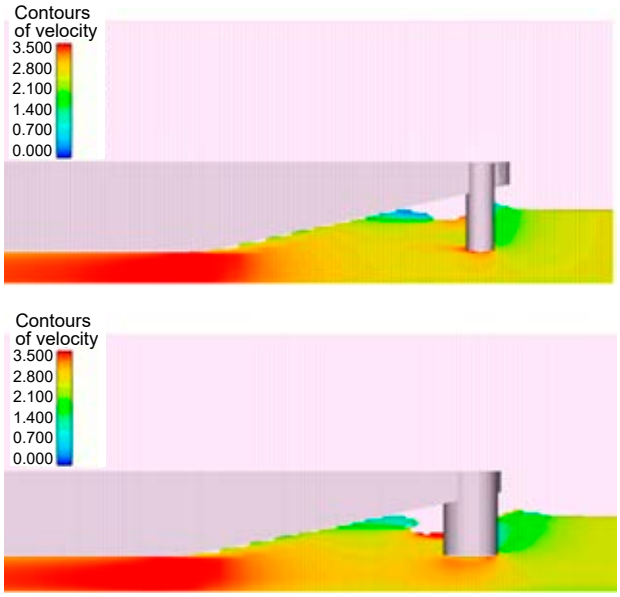

Figure 13. Flow field around rotors v_{barge} = 3 m/s, r = 39 rad/s; a = 0.25 m, α = 4.06 (top); a = 0.465 m, α = 7.5 (bottom)

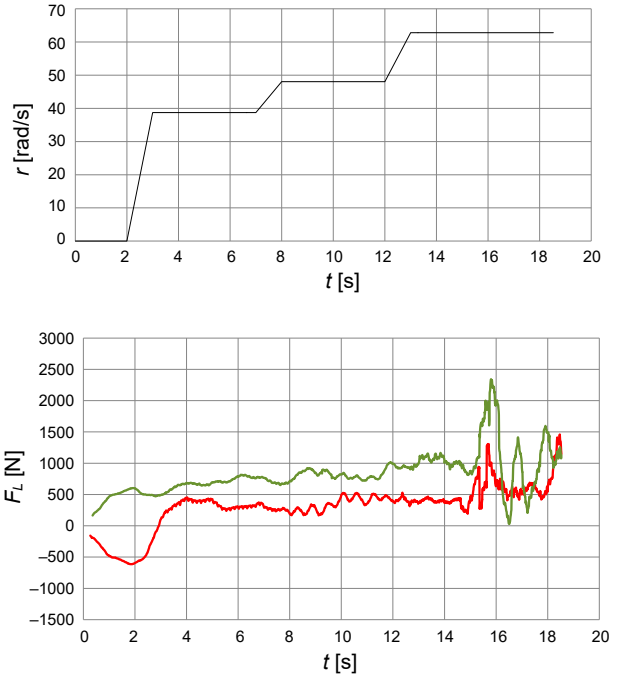

Figure 14. Time series of the rotational speed of rotors and hydrodynamic lift forces generated on the PS (red line) and STB (green line) rotors, a = 0.25 m, v_{barge} = 3 m/s, α values constant over time: α = 4.06, α = 5.21, α = 6.54

Comparison of the parameters influencing the lift force

The lift forces calculated for different inflow velocities and rotational velocities of two rotor diameters are presented in Table 3. ΣF_L is the steering force calculated as a sum of maximum PS and STB rotor lift forces.

Table 3. Lift forces calculated for different combinations of a, v, and r

H	a	H/D	v_{barge}	Re·10^6	r	α	$\lvert F_{Lmean}\rvert$ (CFD)	$\lvert F_{Lmax}\rvert$ (CFD)	ΣF_L (CFD)
m	m	–	m/s	–	rad/s	–	kN	kN	kN
0.77	0.465	1.67	2	1.48	15	4.44	0.3	0.55	0.4
			3	2.22	39	7.5	1.5	3.0	3.7
			4	2.96	39	5.67	4.0	10.0	20.0
					39	4.06	0.8	1.0	1.5
	0.25	3.08	3	1.19	48	5.21	1.0	1.5	3.5
					63	6.54	1.5	3.0	5.0

The maximum steering force was generated at barge velocities of 3 m/s and 4 m/s which corresponded to operational velocities of pushed trains of 10–15 km/h.

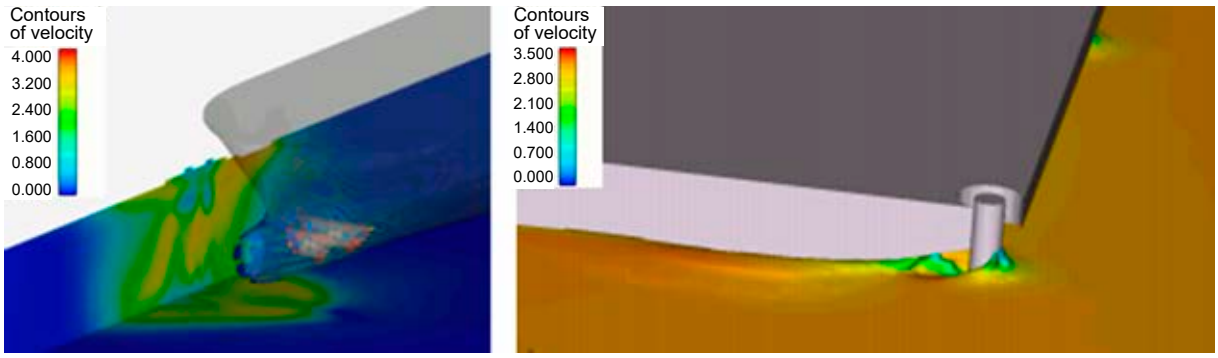

Figure 15. Velocity fields generated by bow thrusters and rotors

Velocity field generated by the bow steering system

The flow fields generated by bow thrusters and rotors are presented in Figure 15.

The bow thruster produced a thrust stream with a constant flow velocity over a distance larger than half of the ship's breadth. In the case of barges, due to the rectangular shape of the bow frames, the outlet opening of the transverse thruster was much closer to the quay wall or riverbank, and the produced thrust stream directly impacted the wall and bottom. The impact of the flow field generated by rotors on the quay walls or banks was different since the high-velocity area was located only near the cylinder surface and depended on the rotor position (Figure 6).

Conclusions

The use of hydrodynamic bow rotors improved the manoeuvrability of pushed trains while navigating inland waterways. The increased turning ability was confirmed by model tests. The manoeuvring space can be reduced due to the reduction of drift angle when turning on a bend and when overtaking and passing other vessels. The ability of a pushed train to maintain its course under a transverse wind can be improved by eliminating leeway and drift.

The presented study was limited to selected parameter ranges due to time-consuming CFD modelling and lack of comparable literature results. However, it allowed the presentation of the influence of rotor diameter, rotor aspect ratio, rotational speed, and inflow velocity on the steering force and provided a direction for future research. The strong influence of the free surface and bow wave on the rotor performance was also observed. The position of a rotor installed in the bow part of a barge determines the inflow velocity and flow restriction, and the inflow velocity to the rotor can be twice less than the speed of the barge. The simulations also showed that the lift force is directly proportional to the rotor radius. The parametric study using CFD simulations confirmed that the steering force generated by rotors at barge velocities of to 3 m/s and 4 m/s, which corresponded to operational velocities of pushed trains of 10–15 km/h, were generated at higher Reynolds numbers of approximately $2.9 \cdot 10^6$.

Acknowledgment

This work was supported by the project: RPPM.01.01.01-22-0068/16-00, "Development of a prototype of a system for monitoring the loads on berths and bed protection in the area of ship berthing along with the implementation of the final product on the market by Enamor Ltd. company from Gdynia" within "Smart Specialisations of Pomerania Region – offshore technology, ports and logistics" – Pomeranian Voivodeship Regional Operational Programme for 2014–2020.

References

1. Abramowicz-Gerigk, T. & Burciu, Z. (2018) Manoeuvring characteristics of the push train with an auxiliary steering device. *Journal of KONES Powertrain and Transport* 25 (2), pp. 7–13.
2. Abramowicz-Gerigk, T., Burciu, Z. & Jachowski, J. (2017) An Innovative Steering System for a River Pushed Train Operated in Environmentally Sensitive Areas. *Polish Maritime Research* 4 (96), 24, pp. 27–34.
3. Catalano, P., Wang, M., Iaccarino, G. & Moin, P. (2003) Numerical simulation of the flow around a circular cylinder at high Reynolds numbers. *International Journal of Heat and Fluid Flow* 24, pp. 463–469.
4. Champmartin, S., Ambari, A. & Roussel, N. (2007) Flow around a confined rotating cylinder at small Reynolds number. *Physics of Fluids* 19, 103101.
5. Dymarski, Cz., Wieliczko, L. & Nalewajski, A. (2003) Project EUREKA Baltecologicalship Eureka/2003 Report, Scientific works 53/SPB, Gdansk University of Technolog. Available from: http://www.pg.gda.pl/~cpdymars/PLIKI/SterStrumEureka.pdf [Accessed: September 20, 2019].

6. Everts, M., Ebrahim R., Kruger, J.P., Miles, E., Sharifpur M. & Meyer, J.P. (2014) *Turbulent flow across a rotating cylinder with surface roughness*. 10th International Conference on Heat Transfer, Fluid Mechanics and Thermodynamics. Orlando, USA.
7. Julien, P.Y. (1997) *River mechanics*. Cambridge University Press 2002. USACE 1997.
8. Karabelas, S.J., Koumroglou, B.C., Argyropoulos, C.D. & Markatos, N.C. (2012) High Reynolds number turbulent flow past a rotating cylinder. *Applied Mathematical Modelling* 36, 1, pp. 379–398.
9. Lantz, J., Sutnikas, A., Breitenbach, S. & Kluge, B. (2018) *Handbook on technical barge concepts for use under BSR specific navigation conditions*. European Project Enhancing Europe Navigation EMMA Report, WP 2, Activity 2. Available from: http://project-emma.eu/sites/default/files/EMMA_Act.%202.2.%20Report_final.pdf [Accessed: September 20, 2019].
10. PIANC (2019) *Design Guidelines for Inland Waterway Dimensions*. PIANC Report InCom WG 141.
11. Pullin, D., Cheng, W. & Samtaney, R. (2018) *Large-eddy simulation of flow about a rotating cylinder at large Reynolds number*. 21st Australasian Fluid Mechanics Conference Adelaide, Australia.
12. Rao, A., Radi, A., Leontini, J.S., Thompson, M.C., Sheridan, J. & Hourigan, K. (2014) A review of rotating cylinder wake transitions. *Journal of Fluids and Structures* 53, pp. 2–14.
13. Yao, Q., Zhou, C.Y. & Wang, C. (2016) *Numerical Study of the Flow past a Rotating Cylinder at Supercritical Reynolds Number*. 4th International Conference on Mechanical Materials and Manufacturing Engineering (MMME 2016).